Journal of Neuroinflammation

RESEARCH

Open Access

PARP9 exacerbates apoptosis and neuroinflammation via the PI3K pathway in the thalamus and hippocampus and cognitive decline after cortical infarction

Mengshi Liao[1,2], Xiya Long[1], Yicong Chen[1], Jiaqi An[1], Weixian Huang[1], Xiangming Xu[1] and Yuhua Fan[1*]

Abstract

Background Cerebral infarction induces substantial neuronal apoptosis and neuroinflammation in the ipsilateral nonischemic thalamus and hippocampus, with a critical correlation to post-stroke cognitive impairment. Poly (ADP-ribose) polymerase 9 (PARP9) has been implicated in apoptosis and inflammation across various diseases, while its role in remote brain damage after cerebral infarction remains unclear. This study aims to investigate the role of PARP9 in mediating neuronal apoptosis and neuroinflammation in remote brain regions after distal middle cerebral artery occlusion (dMCAO) and explore its contribution to secondary brain damage and cognitive decline.

Methods Seventy-four hypertensive rats were randomly assigned to either the sham-operated group or the dMCAO group. The dMCAO group was further subdivided into PARP9 knockdown and overexpression subgroups, with their respective control groups, modulated by adeno-associated viruses (AAV) carrying siScramble, siPARP9, Scramble, or PARP9. Within the PARP9 knockdown subgroup, rats were further treated with either a phosphoinositide 3-kinase (PI3K) inhibitor,2-(4-morpholinyl)-8-phenyl-chromone (LY294002), or vehicle. Spatial learning and memory deficits were evaluated using the Morris water maze test. Secondary neuronal apoptosis and neuroinflammation were quantified 7 days post-dMCAO using Nissl staining, immunofluorescence, immunohistochemistry, TUNEL, and Western blot analysis.

Results PARP9 expression was significantly upregulated in the ipsilateral thalamus and hippocampus after dMCAO, correlating with neuronal apoptosis and neuroinflammation. PARP9 was localized in both neurons and microglia. PARP9 knockdown reduced neuronal apoptosis, neuroinflammation, and microglial activation in the ipsilateral thalamus and hippocampus, and meanwhile improved the cognitive function. In contrast, PARP9 overexpression exacerbated these outcomes. Mechanistically, PARP9 knockdown activated the PI3K pathway, and inhibition of this pathway with LY294002 partially reversed the effects, reinstating neuronal apoptosis, neuroinflammation, and cognitive deficits.

Conclusions Our findings demonstrate that PARP9 aggravates neural damage and cognitive decline after cerebral infarction by promoting neuronal apoptosis and neuroinflammation, partly via the PI3K pathway.

Keywords Cerebral infarction, PARP9, Apoptosis, Neuroinflammation, Thalamus, Hippocampus, Cognition

*Correspondence:
Yuhua Fan
fanyuhua@mail.sysu.edu.cn
Full list of author information is available at the end of the article

Introduction

Cerebral cortical infarction causes immediate ischemic damage and also delayed secondary injury in remote nonischemic brain regions, notably the ipsilateral thalamus and hippocampus [1]. These regions are particularly susceptible to secondary damage after stroke and are strongly associated with long-term neurological deficits and cognitive decline [2, 3]. Unlike the ischemic penumbra, which has a narrow therapeutic window, remote regions undergo gradual injury over several days [1], providing a broader window for interventions to mitigate post-stroke cognitive impairments. Axonal degeneration after cortical infarction disrupts fibral connections to the above remote regions, where secondary neuronal loss and glial proliferation subsequently arise [4, 5]. Neuronal apoptosis, the major secondary neuronal death pathway in remote regions after focal infarction, exacerbates cell loss and compromises network integrity, thus creating an environment vulnerable to further damage [6, 7]. Concurrently, microglial activation amplifies inflammatory responses through the release of pro-inflammatory cytokines, such as interleukin-1β (IL-1β) and tumor necrosis factor-alpha (TNF-α), which further aggravate neuronal degeneration and brain tissue injury [8, 9]. This interplay between apoptosis and neuroinflammation creates a self-perpetuating cycle [10, 11], posing further deterioration to these remote brain regions crucial for cognitive functions. Targeting both apoptotic pathways and neuroinflammation offers a compelling therapeutic approach to mitigate secondary brain damage and to improve the clinical outcome of patients with cerebral infarction.

Poly(ADP-ribose) polymerases (PARP) are enzymes that catalyze the addition of ADP-ribose polymers (PAR) to target proteins, playing crucial roles in DNA repair, apoptosis, and inflammation modulation [12]. Among them, PARP1 has been well studied for its involvement in DNA repair and necrotic cell death pathways, such as parthanatos, which are triggered during ischemic brain injury [13]. While PARP1 inhibitors show promise in ischemic stroke models [14, 15], concerns about off-target effects on non-injured tissues, particularly related to DNA repair, limit their clinical applicability [16]. To address these limitations, research attention has shifted to mono-ADP-ribosyl transferases, such as PARP9 and PARP14, which function independently of DNA repair mechanisms, thus reducing concerns about off-target effects on non-injured tissues [17]. PARP9 and PARP14 collaboratively regulate immune responses and inflammation, with PARP9 playing a proinflammatory role while PARP14 acting as a protective factor in coronary vascular diseases [18]. Notably, PARP14 has shown potential in reducing post-infarction damage by modulating microglial activation [19]. However, its weak expression in the adult mouse brain may limit its neuroprotective capacity [20]. In contrast, PARP9 exhibits high expression in the adult mouse brain [20]. Interestingly, data from the human brain atlas (https://www.proteinatlas.org) reveal that PARP9 and PARP14 have similar expression levels in the human brain, with PARP9 showing slightly higher expression. This suggests potential functional overlap between the two enzymes, particularly in pathological contexts. Although direct evidence in human stroke brains is lacking, studies in glioma patients indicate upregulation of PARP9 [21], supporting its potential involvement in stroke-affected brain regions. PARP9 has been implicated in inflammation and apoptosis in various disease models [18, 21–24], where its elevated expression regulates these processes. In stroke, both inflammation and apoptosis are prominent in remote regions after infarction [1], suggesting that PARP9 may play a role in these mechanisms. However, its involvement in stroke remains largely unexplored. Therefore, this study seeks to determine whether PARP9 contributes to exacerbating secondary damage in remote brain regions after cerebral infarction by mediating apoptosis and neuroinflammation.

The Phosphoinositide 3-kinase (PI3K) signaling pathway is a critical cellular pathway that regulates various physiological processes [25], including cell survival, apoptosis, and inflammation [11, 26, 27]. Its activation after ischemic injuries, such as stroke, has been shown to provide significant neuroprotective effects [28, 29]. In our study, messenger RNA sequencing (mRNA-seq) of ipsilateral thalamus tissues after distal middle cerebral artery occlusion (dMCAO) revealed that PARP9 knockdown led to the activation of the PI3K pathway. Previous studies also have shown that PARP9 plays a critical role in regulating the PI3K pathway in the context of viral infections [24] and cancer [30], suggesting a potential close relationship between PARP9 and this signaling axis. However, while the PI3K pathway has been well-studied in these contexts, the precise mechanisms through which PARP9 exerts its effects, particularly whether it directly influences the PI3K pathway in ischemic stroke, remain unclear. Therefore, further research is needed to investigate the downstream pathways regulated by PARP9 after focal infarction.

In this study, we aim to investigate whether PARP9 plays a role in regulating neuronal apoptosis and neuroinflammation through PI3K signaling pathway in the ipsilateral nonischemic thalamus and hippocampus after focal cortical infarction, and to identify whether PARP9 modulation serves as a potential therapeutic approach to alleviate secondary brain damage and post-stroke cognitive decline.

Methods

Animal

Male Sprague–Dawley (SD) rats, weighing 80–100 g, were sourced from the experimental center of Sun Yat-sen University (License No.: SCXK (Yue) 2021–0029). The rats were housed under specific pathogen-free (SPF) conditions with controlled temperature (22 °C), humidity (50%–60%), and a 12-h light/dark cycle. They had ad libitum access to autoclaved food and purified water. All experimental procedures were approved by the Institutional Animal Care and Use Committee (IACUC) of Sun Yat-sen University, in accordance with guidelines for the care and use of laboratory animals.

Experimental design

This study utilized 80 male SD rats to establish a stroke-prone renovascular hypertensive rat (RHRSP) model, as described previously [31]. After 12 weeks, rats with systolic blood pressure > 180 mmHg and no spontaneous stroke symptoms were selected. The experiment was conducted in three parts: Part 1 aimed to assess baseline responses to dMCAO. Sixteen RHRSP rats were randomly assigned to either a dMCAO group (n = 8) or a sham-operated group (n = 8). Under 1% sodium pentobarbital anesthesia (50 mg/kg, i.p.), dMCAO was performed on the right middle cerebral artery distal to the origin of the striatal branches using bipolar electrocoagulation, while the sham group underwent the same procedure without artery occlusion [32]. Part 2 focused on evaluating the effects of PARP9 modulation. Thirty-six RHRSP rats were randomly divided into four groups: AAV-siScramble (n = 8), AAV-siPARP9 (n = 9), AAV-Scramble (n = 9), and AAV-PARP9 (n = 10). Eight weeks post-RHRSP surgery, rats received stereotactic injections of adeno-associated viruses (AAV) carrying siScramble, siPARP9, Scramble, or PARP9 into the right thalamus and hippocampus. After 12 weeks, all rats underwent dMCAO. Part 3 investigated the role of the PI3K pathway in the neuroprotective effects of PARP9 knockdown. Eighteen rats from the AAV-siPARP9 group that successfully underwent dMCAO were randomly selected for intracerebroventricular infusion of either the PI3K inhibitor, 2-(4-morpholinyl)-8-phenyl-chromone (LY294002), or vehicle (n = 7 per group) using osmotic mini-pumps, with LY294002 administered 24 h post-dMCAO. A total of 24 rats were excluded from the study: six rats failed to develop hypertension, ten rats did not successfully undergo dMCAO, and eight rats died due to anesthesia or post-surgery complications. For additional details, refer to supplementary Figures S1 and S2.

AAV Preparation and stereotaxic injection

Three siRNA sequences targeting rat PARP9 (GenBank: NM_001103351) and a negative control sequence were designed by GeneChem (Shanghai, China) and inserted into GV478 AAV9 vectors containing a CAG-driven EGFP reporter gene and a U6 promoter. Sequence analysis confirmed the constructs, and recombinant AAV was produced by transfecting 293 T cells using Lipofiter™. Viral genome titers were quantified with SYBR Green, yielding an optimal siRNA sequence, AAV-siPARP9 (GCATTAAGACAGTAGCAATTC), with a final titer of 3.05 × 10^12 vg/ml. AAV-siScramble (CGCTGAGTACTTCGAAATGTC) served as a negative control. For PARP9 overexpression, the PARP9 transcript was inserted into the GV467 AAV vector, following the same production and quantification methods, resulting in a viral titer of approximately 3.71 × 10^12 vg/ml. Eight weeks after RHRSP surgery, hypertensive rats with systolic blood pressure ≥ 180 mmHg and no signs of spontaneous stroke were selected for stereotaxic injection of AAV9 into the right thalamus and hippocampus, as previously described [33]. Briefly, after scalp disinfection, a small hole was drilled at specific stereotactic coordinates. AAVs were injected into four sites within the right thalamus and hippocampus using a 15 µl syringe, administering 3 µl per site at an infusion rate of 0.5 µl/min. The coordinates were: − 2.6 mm anteroposterior, 2.6 mm rightwards, and − 7.6 mm and − 7.4 mm dorsoventral; and − 3.0 mm anteroposterior, 2.8 mm rightwards, and − 6.4 mm and − 6.2 mm dorsoventral relative to the bregma. The needle was kept in place for 5 min post-injection to ensure proper diffusion. One month following AAV9 injection, dMCAO surgery was performed to confirm effective gene knockdown or overexpression.

Intracerebroventricular delivery

To inhibit the PI3K pathway, LY294002 was administered intracerebroventricularly via osmotic mini-pumps implanted using stereotactic surgery [34]. LY294002 was diluted in 0.01 M phosphate-buffered saline and delivered into the right lateral ventricle through a 100 µl osmotic mini-pump (Alzet 1003D, Alza Scientific Products) [35]. The infusion was initiated 24 h after dMCAO surgery to prevent interference with the primary effects of the infarct. The stereotactic coordinates for the right lateral ventricle, relative to the bregma, were as follows: − 1.0 mm anteroposterior, 1.5 mm rightward, and − 5.5 mm dorsoventral. The mini-pump delivered LY294002 or vehicle continuously at a rate of 0.5 µl/h over a period of 6 days [36]. After the procedure, the incision was sutured and disinfected, and rats were allowed

to recover with free access to food and water starting 6 h post-surgery. Animals were closely monitored throughout the infusion period for vital signs and overall health.

Behavioral assessments

Spatial cognitive function was assessed using the Morris water maze test from days 3 to 7 post-dMCAO, following a modified protocol based on previous studies [37]. The test included adaptive training, spatial acquisition trials, and a probe trial. On day 3, rats underwent a 3-min free swim to acclimate to the water temperature and environment. Spatial acquisition trials were conducted from days 3 to 6, with a hidden platform placed in quadrant I, submerged 1 cm below the water surface. Each rat was released facing the pool wall and given 60 s to locate and climb onto the platform, completing four trials per day with a 30-min interval between trials. Escape latency and swimming distance were recorded as measures of spatial learning. On day 7, the platform was removed for the probe trial. Rats were released from quadrant III and allowed to swim for 60 s, during which the time spent in quadrant I and the number of platform crossings were recorded to assess spatial memory retention. Motor and sensory functions were evaluated on day 7 using modified Bederson [38] and Garcia scores [39]. The Bederson score assessed limb movement and balance, while the Garcia score evaluated spontaneous activity, symmetry, and tactile responses. Higher scores indicated less severe neurological impairment.

Tissue preparation

Seven days after dMCAO, rats were randomly selected for euthanasia. Deep anesthesia was induced using 1% sodium pentobarbital (50 mg/kg, i.p.), followed by transcardiac perfusion with 200 ml of ice-cold 0.9% saline. After perfusion, the brains were quickly extracted, and the ipsilateral thalamus and hippocampus were isolated, immediately frozen in liquid nitrogen, and stored at − 80 °C for molecular analyses. For histological assessments, the remaining rats underwent an additional perfusion with 200 ml of 4% paraformaldehyde over 15 min. The brains were then post-fixed in 4% paraformaldehyde at 4 °C for 24 h. Coronal Sects. (10 μm thick) were cut using a cryostat (Leica CM1900) for subsequent immunohistochemical analysis.

Nissl staining and immunohistochemistry

Every 50th coronal brain section from bregma + 4.7 mm to − 5.2 mm was stained with 0.3% cresyl violet solution (Beyotime, China) to assess infarct volume [36]. Whole-brain images were captured using an automated digital pathology scanner, and infarct volumes were calculated with K-Viewer V1 software by measuring the areas of the infarcted and contralateral hemispheres. Total infarct volume was expressed as a percentage of the contralateral hemisphere volume. For quantitative analysis in the thalamus and hippocampus, sections between bregma − 2.8 mm and − 4.4 mm were randomly selected. Nissl-stained normal cells were quantified using ImageJ. For immunohistochemistry, sections were incubated with a rabbit anti-PARP9 antibody (1:50, Fine Test, #FNab06160) to assess PARP9 expression in the ipsilateral thalamus and hippocampus. The mean optical density of PARP9 in the ipsilateral thalamus and hippocampus was calculated.

Immunofluorescence

Immunofluorescence was performed on coronal brain sections to evaluate the expression and co-localization of markers, including PARP9, NeuN (neuronal marker), Iba-1 (microglial marker), GFAP (astrocyte marker), cleaved caspase-3 (CC3, apoptosis marker), CD86 (pro-inflammatory microglial marker), and CD163 (anti-inflammatory microglial marker). Sections were incubated with the following primary antibodies: rabbit anti-PARP9 (1:50, Fine Test, #FNab06160), rabbit anti-CC3 (1:50, CST, #9664), rabbit anti-CD86 (1:100, Genetech, #GTX32507), rabbit anti-CD163 (1:50, Genetech, #ab182422), mouse anti-NeuN (1:200, Millipore, #MAB377), mouse anti-Iba-1 (1:200, Abcam, #ab283319), and mouse anti-GFAP (1:400, CST, #3670). After washing with PBS, sections were incubated with Alexa Fluor-conjugated secondary antibodies, followed by counterstaining with DAPI (4′,6-diamidino-2-phenylindole) to visualize nuclei. Images were captured using a confocal microscope, and quantification of stained cells was performed using ImageJ software. Neurons and microglia were counted, and the percentages of double-positive cells were calculated to assess apoptosis and microglial activation. Specifically, $CC3^{+}NeuN^{+}$ cells were used to evaluate neuronal apoptosis, while $CD86^{+}Iba\text{-}1^{+}$ cells were quantified to assess pro-inflammatory microglial activation, and $CD163^{+}Iba\text{-}1^{+}$ cells to assess anti-inflammatory microglial activation.

TUNEL staining

Neuronal apoptosis was assessed using the Terminal deoxynucleotidyl transferase dUTP nick end labeling (TUNEL) assay with the In-situ TUNEL Apoptosis Detection Kit (Roche, Switzerland). Brain sections were counterstained with DAPI to label nuclei and then imaged using a fluorescence microscope (Nikon, Japan). TUNEL-positive neurons, representing apoptotic cells, were quantified using ImageJ software.

RNA sequencing analysis

Total RNA was isolated from the ipsilateral thalamus of rats 7 days after dMCAO using the Trizol reagent (Invitrogen, USA), with chloroform and isopropanol for phase separation and RNA precipitation. RNA quality and quantity were determined using NanoDrop 2000 and Agilent 2100 Bioanalyzer. For mRNA enrichment, polyA-tail specific magnetic beads and Oligo(dT) were used. Double-stranded cDNA was synthesized and amplified via PCR using specific primers. The resulting PCR products were denatured into single-stranded DNA, which was subsequently cyclized into a circular library using bridge primers. For miRNA library construction, 20-nt fragments were selected, including non-coding RNAs such as rRNA, tRNA, and siRNA. Sequencing was performed on the DNBSEQ platform (BGI Genomics, Shenzhen, China) [40]. Differential expression analysis was conducted with a significance threshold of $p < 0.05$ and $|\log2(\text{fold change})| \geq 1$. Detailed descriptions of the datasets and results are provided in the results section. Bioinformatic analyses were performed using the Dr.Tom platform (https://biosys.bgi.com/#/report/login), developed by BGI Genomics.

Immunoblotting analysis

Protein samples from the ipsilateral thalamus and hippocampus were extracted using RIPA lysis buffer (Thermo Scientific, USA), supplemented with protease and phosphatase inhibitors. Protein concentrations were determined using the Pierce BCA Protein Assay Kit (Thermo Scientific, USA). Equal amounts of protein (30 μg) were separated by 10% SDS-PAGE and transferred to PVDF membranes (Millipore, USA). Membranes were blocked with 5% BSA in TBST and incubated overnight at 4 °C with primary antibodies, including: rabbit anti-PARP9 (1:500, Fine Test, #FNab06160), rabbit anti-Bax (1:500, Abcam, #ab32503), rabbit anti-Bcl-2 (1:1000, Abcam, #ab182858), rabbit anti-Cleaved Caspase-9 (CC9, 1:500, CST, #9507), rabbit anti-Caspase-9 (1:1000, CST, #9508), rabbit anti-TNF-α (1:500, Affinity, #AF7014), rabbit anti-IL-1β (1:500, Affinity, #AF5103), rabbit anti-phospho-PI3K p85 (p-PI3K, 1:1000, CST, #17,366), rabbit anti-PI3K p85 (1:1000, CST, #4257), rabbit anti-phospho-AKT (p-AKT, 1:1000, CST, #9271), rabbit anti-AKT (1:1000, CST, #9272), rabbit anti-phospho-mTOR (p-mTOR, 1:1000, CST, #2971), rabbit anti-mTOR (1:1000, CST, #2983), rabbit anti-GAPDH (1:1000, CST, #2118), and mouse anti-α-tubulin (1:1000, CST, #2125). After incubation, membranes were treated with HRP-conjugated secondary antibodies, and the bands were detected using enhanced chemiluminescence (ECL) reagents. Visualization was performed using the Bio-Rad ChemiDoc imaging system, and band intensities were quantified using ImageJ software, with normalization to α-tubulin or GAPDH.

Statistical analysis

Data were analyzed using GraphPad Prism (version 9.0.2) and are presented as mean ± standard error of the mean (SEM). Comparisons between two groups were performed using an unpaired Student's t-test, while comparisons among three or more groups were conducted using one-way analysis of variance (ANOVA) followed by post hoc multiple comparison tests. Each experimental group included at least three biological replicates, and statistical significance was defined as $p < 0.05$.

Results

Increased neuronal apoptosis and neuroinflammation in the ipsilateral thalamus and hippocampus after cerebral cortical infarction

Nissl staining confirmed that the infarction in the dMCAO group was localized to the right somatosensory cortex (Supplementary Figure S3A). Behavioral testing revealed significant cognitive deficits in the dMCAO group, with delayed escape latency and reduced time spent in the target quadrant during the Morris water maze, indicating impairments in spatial learning and memory (Supplementary Figure S3B). Motor and sensory impairments in the dMCAO group were also evident, as indicated by the Bederson and Garcia scores (Supplementary Figure S3E, F). Furthermore, the dMCAO group showed reduced Nissl-positive neurons in the ipsilateral thalamus and hippocampal CA3 region, indicating secondary neuronal damage (Supplementary Figure S3C, D).

Immunofluorescence staining showed an increase in the number of cleaved caspase-3 (CC3)-positive neurons and a decrease in the number of NeuN-positive cells in the ipsilateral thalamus 7 days post-dMCAO compared to the sham-operated group ($p < 0.05$, Fig. 1A). These findings indicate enhanced neuronal apoptosis in the dMCAO group. Western blot analysis confirmed this conclusion, showing elevated levels of Cleaved Caspase-9 (CC9) and the pro-apoptotic protein Bax, and meanwhile a decrease of the anti-apoptotic protein Bcl-2 in the ipsilateral thalamus of the dMCAO group ($p < 0.05$, Fig. 1C). Similar apoptotic results were also observed in the ipsilateral hippocampus, characterized by elevated expression of apoptotic markers and reduced $NeuN^+$ neuron in the CA3 region (Supplementary Figure S4A), further confirmed by western blot analysis (Supplementary Figure S4C).

Neuroinflammation was also elevated in the dMCAO group. The number of pro-inflammatory microglia was significantly increased in the ipsilateral thalamus, along with elevated levels of inflammatory cytokines IL-1β

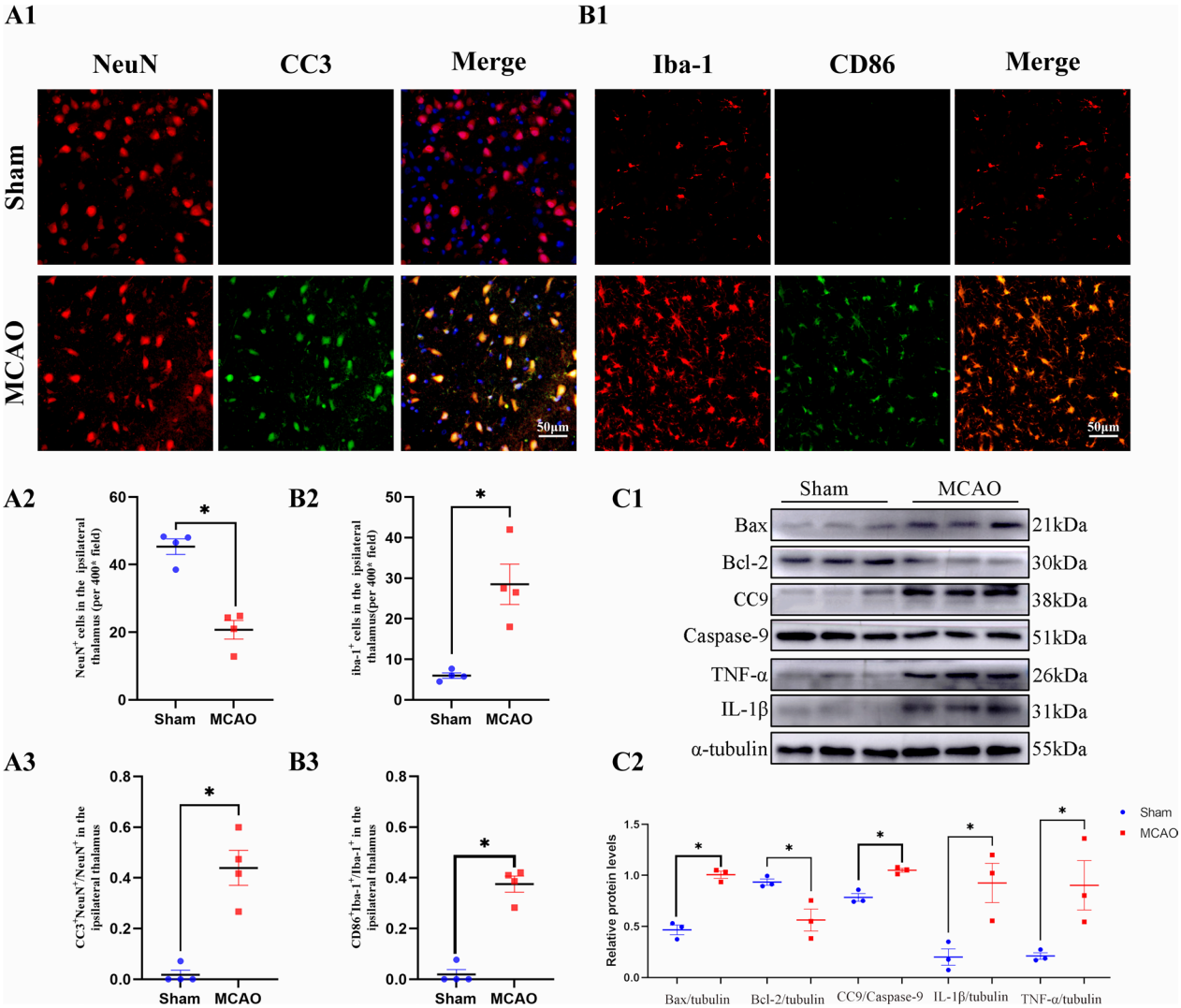

Fig. 1 Neuronal apoptosis and neuroinflammation in the ipsilateral thalamus after dMCAO. (**A1**, **B1**) Representative immunofluorescence images showing co-localization of cleaved caspase-3 (CC3, green), NeuN (red), and DAPI (blue), and separate co-localization of CD86 (green) with Iba-1 (red) in the ipsilateral thalamus of sham-operated and dMCAO rats. Scale bar = 50 μm, n = 4 per group. (**A2**-**A3**, **B2**-**B3**) Quantitative analysis of NeuN-positive neurons ($NeuN^+$), CC3-positive neurons ($CC3^+NeuN^+$), Iba-1-positive microglia ($Iba\text{-}1^+$), and CD86-positive microglia ($CD86^+Iba\text{-}1^+$) in the ipsilateral thalamus, with comparison to sham-operated groups. (**C1**) Western blot analysis of cleaved caspase-9 (CC9), caspase-9, Bax, Bcl-2, TNF-α, and IL-1β protein levels in the ipsilateral thalamus of sham-operated and dMCAO rats (n = 3 per group). (**C2**) Semi-quantitative analysis of protein expression levels, with CC9 normalized to caspase-9, and Bax, Bcl-2, TNF-α, and IL-1β normalized to α-tubulin. Data are presented as mean ± SEM. *$p < 0.05$, compared to the sham-operated group

and TNF-α, compared to the Sham group ($p < 0.05$, Fig. 1B, C). Similar neuroinflammatory changes were observed in the ipsilateral hippocampus of the dMCAO group (Supplementary Figure S4B, C), further supporting the widespread activation of neuroinflammation after cerebral cortical infarction. Our results show an increase in anti-inflammatory microglia in the ipsilateral thalamus and hippocampal CA3 region after dMCAO compared to the sham group ($p < 0.05$, Supplementary Figure S4D, E).

Spatial expression profiles of PARP9 in the ipsilateral thalamus and hippocampus after cerebral cortical infarction

Seven days after dMCAO, western blot analysis of the ipsilateral thalamus and hippocampus tissue both revealed a significant upregulation of PARP9 levels in the dMCAO group compared to the sham-operated group ($p < 0.05$, Fig. 2B; Supplementary Figure S5A). Compared to the sham group, PARP9 expression was significantly increased in the ipsilateral thalamus and hippocampus

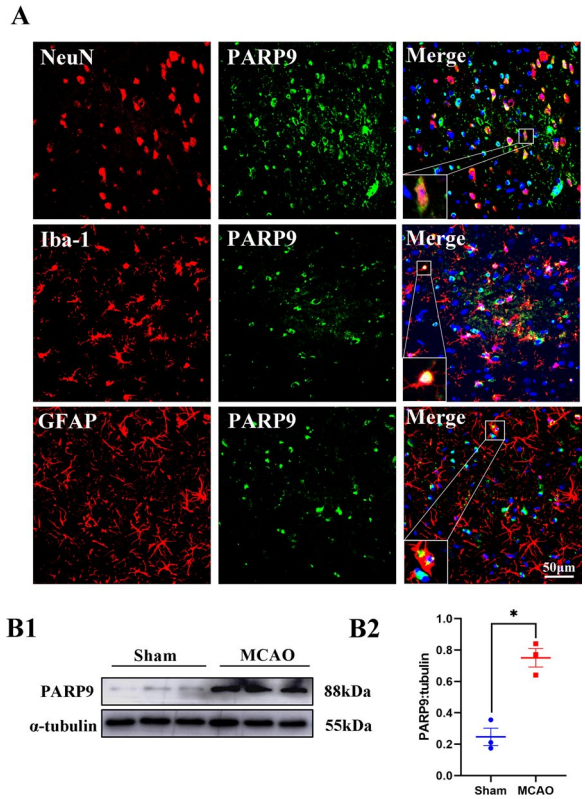

Fig. 2 Co-localization of PARP9 in different cell types in the ipsilateral thalamus after dMCAO. **A** Representative immunofluorescence images showing the co-localization of PARP9 (green) with NeuN$^+$ neurons, Iba-1$^+$ microglia, GFAP$^+$ astrocytes (red), and DAPI (blue) in the ipsilateral thalamus 7 days post-dMCAO. Insets highlight areas of PARP9 expression within NeuN$^+$, Iba-1$^+$, and GFAP$^+$ cells. Scale bar = 50 μm. (**B1**) Western blot analysis showing PARP9 expression levels in the ipsilateral thalamus of sham-operated and dMCAO groups. (**B2**) Quantitative analysis of PARP9 expression normalized to α-tubulin in both groups. n = 3 per group. Data are presented as mean ± SEM. *p < 0.05, compared with the sham-operated group

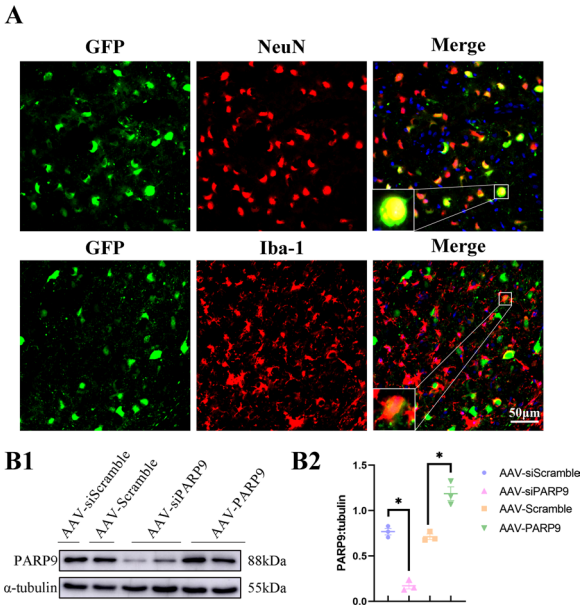

Fig. 3 AAV-mediated knockdown and overexpression of PARP9 in the ipsilateral thalamus after dMCAO. **A** Immunofluorescence images showing co-localization of GFP (green) with NeuN (red), Iba-1 (red), and DAPI (blue) in the ipsilateral thalamus. Scale bar = 50 μm. (**B1**-**B2**) Western blot images showing PARP9 and α-tubulin expression in the ipsilateral thalamus from AAV-siScramble, AAV-siPARP9, AAV-Scramble, and AAV-PARP9 groups, with semi-quantitative analysis of PARP9 expression relative to α-tubulin. n = 3 per group. Data are presented as mean ± SEM. *p < 0.05, compared with respective control groups

at 3, 7, and 14 days post-dMCAO. Specifically, PARP9 expression peaked at 7 days in the ipsilateral thalamus and at 3 days in the ipsilateral hippocampus ($p < 0.05$, Supplementary Figure S5B, C). Immunohistochemical analysis further corroborated these findings, showing a pronounced increase in the mean optical density of PARP9 in the ipsilateral thalamus and hippocampus 7 days post-dMCAO compared with the sham-operated rats ($p < 0.05$, Supplementary Figure S5D). Furthermore, double immunofluorescence staining revealed that PARP9 was predominantly expressed in NeuN-labeled neurons, with lower levels observed in the Iba-1-labeled microglia and GFAP-labeled astrocytes within the ipsilateral thalamus 7 days after dMCAO (Fig. 2A). Collectively, these data suggest that PARP9 may contribute to pathological changes of neurons and glial cells in remote brain regions after cerebral cortical infarction.

Effects of PARP9 knockdown or overexpression on cognitive function and secondary damage in the ipsilateral thalamus and hippocampus after cerebral cortical infarction

To investigate the role of PARP9 in cognition function and secondary brain damage in the ipsilateral thalamus and hippocampus, we used AAV-mediated modulation of PAPR9. To ensure effective viral transfection, AAV-siPARP9, AAV-siScramble, AAV-PARP9, or AAV-Scramble containing a CAG-driven EGFP reporter gene were stereotactically delivered to the right thalamus and hippocampus 8 weeks after RHRSP induction. Seven days after dMCAO, GFP-fluorescence was detected to be distributed within the ipsilateral thalamus and hippocampus, confirming successful transfection (Supplementary Figure S6A). GFP-tagged AAV-siPARP9 predominantly colocalized with NeuN$^+$ neurons, with minimal expression in Iba-1$^+$ microglia (Fig. 3A). Western blot results indicated a significant reduction in PARP9 expression in the ipsilateral thalamus in the AAV-siPARP9 group compared to AAV-siScramble. Conversely, the AAV-PARP9 group exhibited elevated PARP9 levels in comparison with AAV-Scramble controls (Fig. 3B). Similar results

were observed in the ipsilateral hippocampus across groups, as validated by immunofluorescence co-localization and western blot analysis (Supplementary Figure S6B, C).

The Morris water maze tests indicated that rats in the AAV-siPARP9 group exhibited shorter escape latencies in locating the hidden platforms compared to the AAV-siScramble controls on days 5–6 after dMCAO ($p < 0.05$). Conversely, rats treated with AAV-PARP9 showed no significant differences in escape latency compared to AAV-Scramble from days 4–6 after dMCAO. During the probe trial on day 7, rats treated with AAV-siPARP9 spent more time in the target quadrant and crossed the platform location more frequently ($p < 0.05$), while no significant difference was observed in the AAV-PARP9 group compared to their control groups (Fig. 4A; Supplementary Figure S7A). Swimming velocity did not significantly differ among all the groups, suggesting that motor function was unaffected by the AAV treatments (Supplementary Figure S7B). Further evaluations of motor and sensory functions using Bederson and Garcia scores revealed no significant differences among the groups (all $p > 0.05$), indicating that PARP9 modulation had minimal impact on motor and sensory functions after dMCAO (Supplementary Figure S7C, D). Nissl staining revealed a significantly higher number of intact Nissl-positive neurons in the ipsilateral thalamus and hippocampus of the AAV-siPARP9 group compared to the AAV-siScramble group. Conversely, the AAV-PARP9 group exhibited a reduced number of intact neurons in these regions compared with the AAV-Scramble controls ($p < 0.05$, Fig. 4B, C). Nevertheless, there were no significant changes in infarct volume among the groups ($p > 0.05$), suggesting that PARP9 modulation has no effect on infarct size (Fig. 4D). Overall, these findings suggest that PARP9 knockdown mitigates neuronal loss and promotes cognitive recovery, while PARP9 overexpression exacerbates neuronal damage and tends to worsen cognitive function, though this effect was not statistically significant after cerebral cortical infarction.

Effect of PARP9 knockdown or overexpression on neuronal apoptosis in the ipsilateral thalamus and hippocampus after cerebral cortical infarction

To investigate the role of PARP9 in neuronal apoptosis, TUNEL and CC3 staining were performed in the ipsilateral thalamus and hippocampus after dMCAO. The AAV-siPARP9 group exhibited a significant reduction in the number of TUNEL-positive cells and CC3-positive neurons in the ipsilateral thalamus compared to the AAV-siScramble controls ($p < 0.05$). Conversely, the AAV-PARP9 group showed an increase in TUNEL-positive cells and CC3-positive neurons compared to the AAV-Scramble group ($p < 0.05$, Fig. 5A, B). Similar results were found in the ipsilateral hippocampus, where the AAV-siPARP9 group demonstrated reduced apoptotic markers, while the AAV-PARP9 group exhibited increased TUNEL-positive and CC3-positive neurons ($p < 0.05$, Supplementary Figure S8A, B). Western blot analysis of thalamus tissue confirmed these results, revealing decreased Caspase-9 activation and Bax expression, alongside increased Bcl-2 levels in the AAV-siPARP9 group compared to the AAV-siScramble group (all $p < 0.05$). In contrast, the AAV-PARP9 group displayed significantly elevated Bax expression but no changes in Caspase-9 activation or Bcl-2 levels (Fig. 5C). These trends were generally consistent in the ipsilateral hippocampus, where the AAV-siPARP9 group exhibited reduced Caspase-9 activation and Bax expression alongside increased Bcl-2 levels, while no significant difference was detected in the AAV-PARP9 group compared to the AAV-Scramble group (all $p > 0.05$, Supplementary Figure S8C). Overall, the above results reveal the role of PARP9 modulation in the neuronal apoptosis in remote nonischemic regions after cerebral infarction.

Effect of PARP9 knockdown or overexpression on neuroinflammation in the ipsilateral thalamus and hippocampus after cerebral cortical infarction

To investigate the effects of PARP9 modulation on neuroinflammation after cerebral cortical infarction, immunofluorescence analysis was conducted to assess pro-inflammatory microglial activation in the ipsilateral thalamus and hippocampus. The AAV-siPARP9 group exhibited a significant reduction in both total microglia (Iba-1$^+$) and pro-inflammatory microglia (CD86$^+$Iba-1$^+$), along with an increase in anti-inflammatory microglia (CD163$^+$Iba-1$^+$) in the ipsilateral thalamus compared to the AAV-siScramble group ($p < 0.05$). In contrast, the AAV-PARP9 group showed an increase in total microglia ($p < 0.05$), no significant change in pro-inflammatory microglia and a decrease in anti-inflammatory microglia ($p < 0.05$) compared to the AAV-Scramble group (Fig. 6A, B). A similar trend was observed in the ipsilateral hippocampal CA3 region, where the AAV-siPARP9 group showed a trend toward reduced total microglia ($p > 0.05$) and pro-inflammatory microglia counts ($p < 0.05$), with an increase in anti-inflammatory microglia ($p < 0.05$), while the AAV-PARP9 group exhibited an increase in total microglia ($p < 0.05$) and anti-inflammatory microglia ($p < 0.05$), with no significant change in pro-inflammatory microglia compared to the control groups (Supplementary Figure S9A, B). Western blot analysis confirmed these findings, revealing significantly lower levels of pro-inflammatory cytokines, including TNF-α and IL-1β, in the AAV-siPARP9 group compared

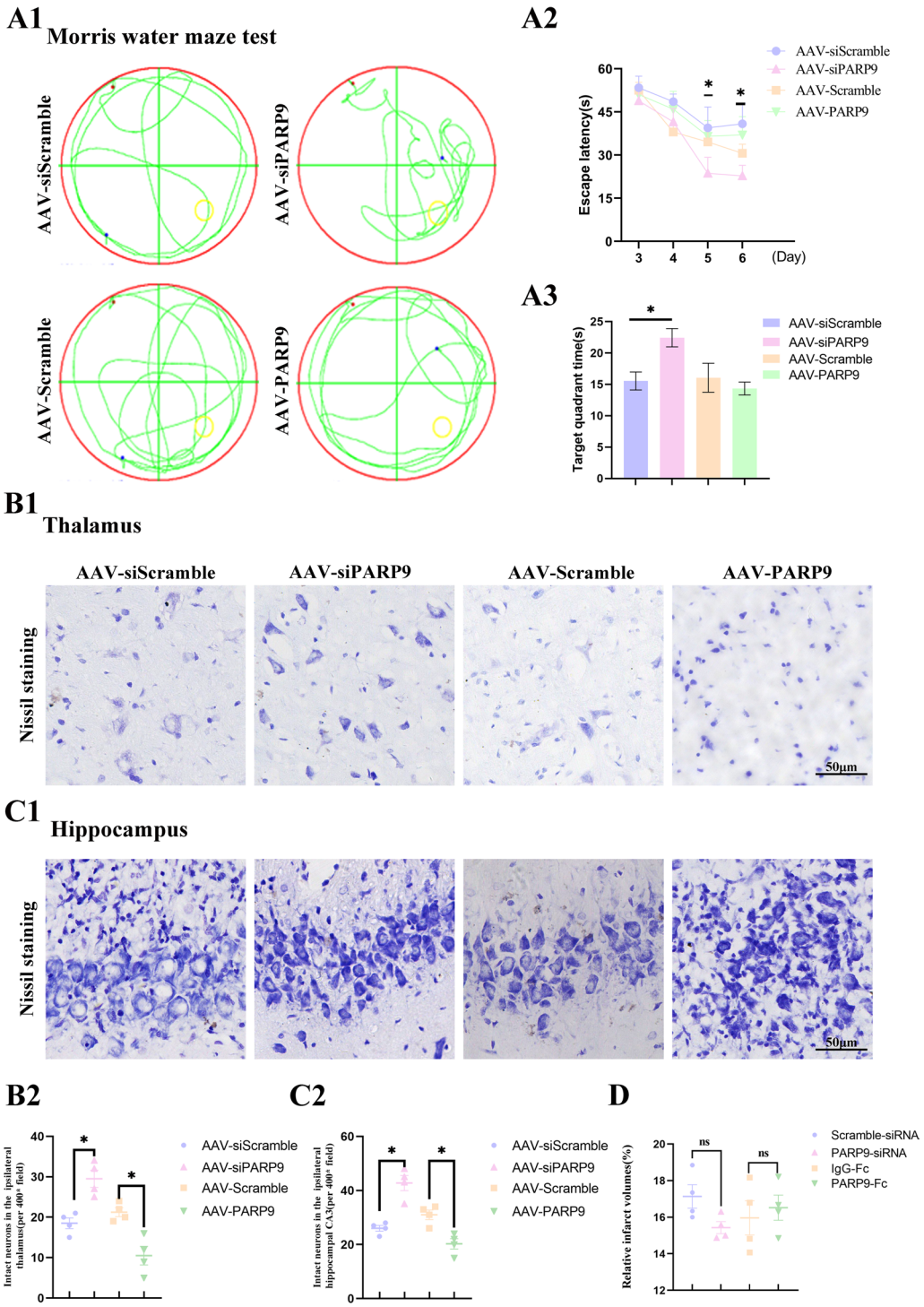

Fig. 4 Effects of PARP9 knockdown or overexpression on cognitive function and secondary damage in the ipsilateral thalamus and hippocampus after dMCAO. (**A1**) Representative swimming trajectories in the Morris water maze for the AAV-siScramble, AAV-siPARP9, AAV-Scramble, and AAV-PARP9 groups (n = 7 per group). (**A2**) Statistical analysis of average escape latencies across the four groups from days 3 to 6 post-dMCAO. (**A3**) Time spent in the target quadrant on day 7 post-dMCAO. (**B1**, **C1**) Representative Nissl staining images of the ipsilateral thalamus and hippocampal CA3 region across the four groups (n = 4 per group). Scale bar = 50 μm. (**B2**, **C2**) Semi-quantitative analysis of Nissl + neurons in the ipsilateral thalamus and hippocampal CA3 region across the four groups. **D** Relative infarct volume (%) across the four groups post-dMCAO. Data are presented as mean ± SEM. *p < 0.05 compared to the respective negative control group

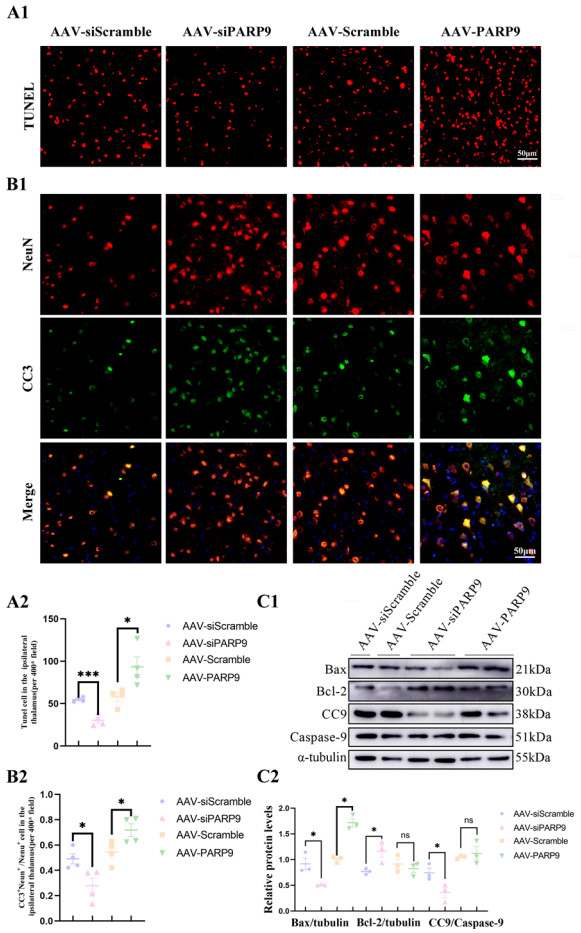

Fig. 5 Effects of PARP9 knockdown or overexpression on neuronal apoptosis in the ipsilateral thalamus after dMCAO. (**A1**, **B1**) Representative images of TUNEL staining and co-immunofluorescence staining for cleaved caspase-3 (CC3, green), NeuN (red), and DAPI (blue) in the ipsilateral thalamus across the AAV-siScramble, AAV-siPARP9, AAV-Scramble, and AAV-PARP9 groups (n = 4 per group). Scale bar = 50 μm. (**A2**, **B2**) Quantitative analysis of TUNEL-positive cells and CC3-positive neurons in the ipsilateral thalamus. (**C1**) Representative Western blot images showing expression levels of cleaved caspase-9 (CC9), total caspase-9, Bax, Bcl-2, and α-tubulin in the ipsilateral thalamus at 7 days after dMCAO across the groups. (**C2**) Semi-quantitative analysis of CC9 normalized to total caspase-9, and Bax and Bcl-2 normalized to α-tubulin. n = 3 per group. Data are presented as mean ± SEM. *p < 0.05, compared with the respective scramble control group

to the AAV-siScramble group in the ipsilateral thalamus ($p < 0.05$). In the AAV-PARP9 group, cytokine levels were comparable to those of the AAV-Scramble group in the ipsilateral thalamus (Fig. 6C). Consistent results of western blot were observed in the ipsilateral hippocampus, with the AAV-siPARP9 group showing reduced cytokine expression, while the AAV-PARP9 group exhibited no significant difference compared to controls (Supplementary Figure S9C). Collectively, these findings suggest that PARP9 knockdown effectively attenuates microglial activation and reduces neuroinflammation in the ipsilateral thalamus and hippocampus, whereas PARP9 overexpression does not significantly impact the neuroinflammatory response in remote regions after cerebral cortical infarction.

PARP9 knockdown alleviates neuronal apoptosis, neuroinflammation, and cognitive deficits via the PI3K pathway

To investigate the mechanisms through which PARP9 accelerates neuronal apoptosis and neuroinflammation after dMCAO, we performed mRNA-seq on the ipsilateral thalamus of AAV-siScramble and AAV-siPARP9 rats 7 days after dMCAO to identify potential target pathways. In our study, mRNA-seq and Kyoto Encyclopedia of Genes and Genomes (KEGG) enrichment analysis revealed that after PARP9 knockdown, the PI3K pathway was prominently activated (Fig. 7A). This finding was further confirmed by increased phosphorylation levels of PI3K, AKT, and mTOR in the ipsilateral thalamus of AAV-siPARP9 rats compared to controls (Fig. 7B), with similar results found in the ipsilateral hippocampus (Supplementary Figure S11A). Though other pathways, including Ras, MAPK, and cAMP, were also activated, the PI3K pathway stands out due to its critical role in apoptosis and inflammation [11, 26, 27]. Furthermore, given the established association between PARP9 and the PI3K pathway [24, 30], we chose to focus our investigation on this pathway, while acknowledging the potential contribution of the other pathways in mediating the observed effects.

To validate the role of PI3K activation in mediating the neuroprotective effects of PARP9 knockdown, we administered the PI3K inhibitor LY294002 intracerebroventricularly to AAV-siPARP9 rats. LY294002 effectively blocked PI3K pathway activation, as evidenced by reduced phosphorylation of AKT and mTOR ($p < 0.05$, Fig. 7C). Notably, LY294002 treatment reversed the neuroprotective effects of PARP9 knockdown, as shown by increased Caspase-9 activation, upregulated Bax expression, downregulated Bcl-2, and elevated levels of IL-1β and TNF-α in the ipsilateral thalamus of siPARP9-LY294002 rats compared to the siPARP9-vehicle group ($p < 0.05$, Fig. 7C). Similar results found in the ipsilateral hippocampus (Supplementary Figure S11B). In the Morris water maze test, siPARP9-LY294002 rats exhibited significantly longer escape latencies on day 7 compared to the siPARP9-vehicle group ($p < 0.05$). During the probe trial, these rats crossed the platform location fewer times and spent less time in the target quadrant, although the reduction in target quadrant time did not

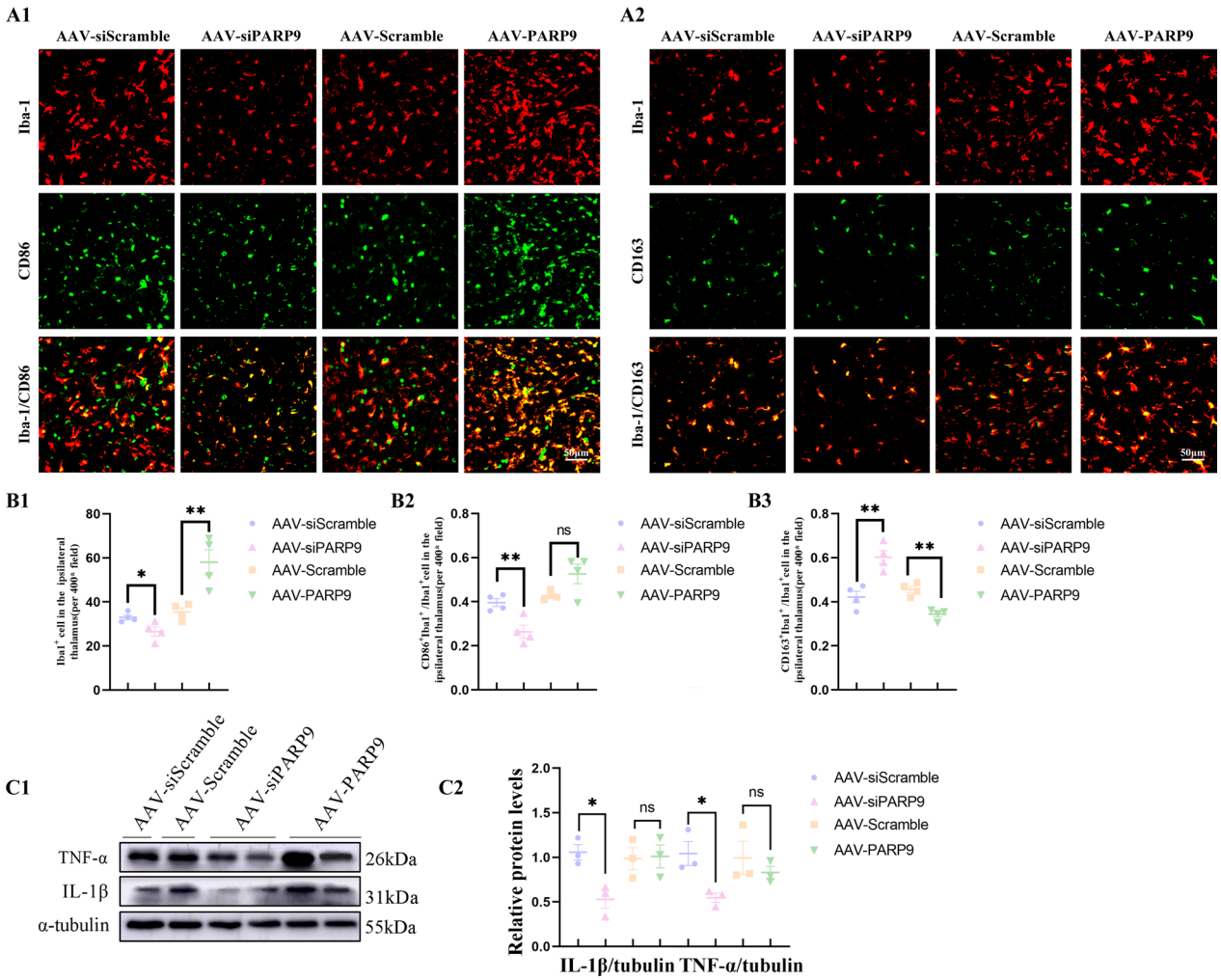

Fig. 6 Effects of PARP9 knockdown or overexpression on neuroinflammation in the ipsilateral thalamus after dMCAO. (**A1**, **A2**) Representative immunofluorescence images showing co-staining of Iba-1 (red) with CD86 (green) and CD163 (green) in the ipsilateral thalamus across AAV-siScramble, AAV-siPARP9, AAV-Scramble, and AAV-PARP9 groups (n = 4 per group). Scale bar = 50 μm. (**B1**-**B3**) Quantitative analysis of total microglial counts (Iba-1$^+$), CD86-positive microglia (CD86$^+$Iba-1$^+$), and CD163-positive microglia (CD163$^+$Iba-1$^+$) in the ipsilateral thalamus across the four groups. (**C1**) Representative Western blot images showing IL-1β, TNF-α, and α-tubulin expression in the ipsilateral thalamus 7 days after dMCAO across the four groups. (**C2**) Semi-quantitative analysis of IL-1β and TNF-α protein levels, normalized to α-tubulin. n = 3 per group. Data are presented as mean ± SEM. *p < 0.05, compared to the respective scramble control group

(See figure on next page.)

Fig. 7 Inhibition of the PI3K pathway reverses the neuroprotective effects of PARP9 knockdown after dMCAO. **A** KEGG pathway enrichment bubble chart highlighting PI3K pathway enrichment following PARP9 knockdown. (**B1**) Western blot images showing phosphorylated PI3K (p-PI3K), total PI3K, phosphorylated AKT (p-AKT), total AKT, phosphorylated mTOR (p-mTOR), total mTOR, and GAPDH expression in the ipsilateral thalamus across AAV-siScramble, AAV-siPARP9, AAV-Scramble, and AAV-PARP9 groups (n = 3 per group). (**B2**) Quantitative analysis of p-PI3K, p-AKT, and p-mTOR expression normalized to total protein levels across four groups. (**C1**) Western blot images showing expression of p-AKT, total AKT, p-mTOR, total mTOR, Bax, Bcl-2, cleaved caspase-9 (CC9), total Caspase-9, TNF-α, IL-1β, and α-tubulin in the ipsilateral thalamus for siPARP9-vehicle and siPARP9-LY294002 groups (n = 3 per group). (**C2**–**C3**) Semi-quantitative analysis of p-AKT, p-mTOR, and CC9 expression normalized to total protein, while Bax, Bcl-2, TNF-α, and IL-1β were normalized to α-tubulin levels. (**D1**) Morris water maze trajectories for siPARP9-vehicle and siPARP9-LY294002 groups (n = 7 per group), showing spatial learning post-dMCAO. (**D2**) Quantitative analysis of escape latency from days 3 to 6 in the Morris water maze. (**D3**) Time spent in the target quadrant during the day 7 probe trial. Data are presented as mean ± SEM. *p < 0.05 compared to vehicle-treated groups

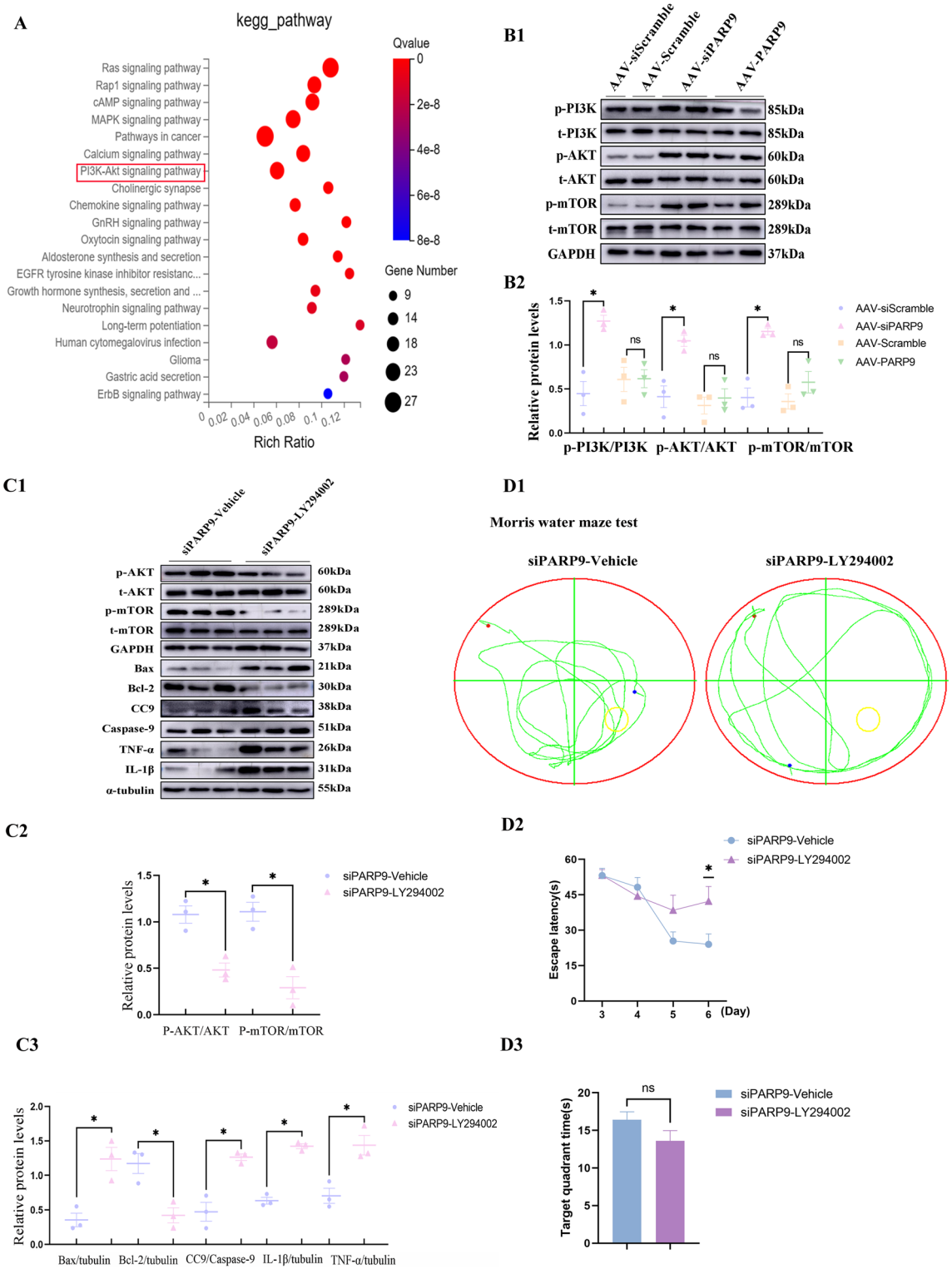

Fig. 7 (See legend on previous page.)

reach statistical significance ($p > 0.05$, Fig. 7D; Supplementary Figure S10A). Swimming speeds remained consistent across all groups, confirming that the observed cognitive impairments were not attributable to motor deficits (Supplementary Figure S10B). Motor and sensory evaluations using Bederson and Garcia scores showed no

significant differences between siPARP9-LY294002 and siPARP9-vehicle groups ($p > 0.05$, Supplementary Figure S10C, D). Together, these data demonstrate that knockdown of PARP9 suppresses apoptosis and neuroinflammation, partially mediated by the activation of the PI3K pathway.

Discussion

In this study, we explored the role of PARP9 in mediating neuronal apoptosis and neuroinflammation and its underlying mechanisms in secondary damage after cerebral cortical infarction in hypertensive rats. We found that (1) PARP9 expression is significantly elevated in the ipsilateral thalamus and hippocampus post-dMCAO, coinciding with increased neuronal apoptosis and neuroinflammation; (2) PARP9 knockdown alleviates neuronal apoptosis and microglial activation, thereby improving neuronal survival and cognitive function, whereas its overexpression exacerbates these detrimental effects; and (3) the neuroprotective effects of PARP9 knockdown are mediated, at least in part, through the PI3K signaling pathway, as inhibition of this pathway with LY294002 reverses these benefits. Taken together, these results suggest that PARP9 aggravates neural damage and cognitive decline after cerebral infarction by promoting neuronal apoptosis and neuroinflammation, partly via the PI3K pathway (Fig. 8).

Focal cortical infarction within the MCA territory was induced in hypertensive rats in our study, which simulates one of the most important etiologies of stroke patients, and on the other hand confines the infarct focus to cortical regions, sparing the thalamus and hippocampus from direct ischemic attack [32]. Neuronal apoptosis and neuroinflammation in the ipsilateral thalamus and hippocampus are major contributors to secondary injury in remote nonischemic brain regions and cognitive impairment after cerebral cortical infarction [1, 8, 41]. Although previous studies have separately investigated apoptosis [6, 7] and neuroinflammation [8, 9, 42] in secondary brain regions, the factors activated by stroke that simultaneously trigger both processes remain largely unknown. Our study demonstrates that the stroke-induced increase in PARP9 plays a key role in mediating both apoptosis and neuroinflammation in the ipsilateral thalamus and hippocampus after focal cortical infarction. Our results show that PARP9 is predominantly expressed in neurons, with relatively low levels in microglia. Although PARP9 knockdown primarily affects neurons, it also leads to changes in microglial polarization. We cannot rule out the possibility that alterations in microglial PARP9 expression itself may influence its polarization. Furthermore, we suggest that PARP9 may regulate microglial polarization through complex cell interactions, particularly through bidirectional signaling between neurons and microglia [43, 44]. However, the exact molecular mechanisms by which PARP9 modulates microglial polarization, and whether through changes in protein expression, mRNA levels, post-translational modifications, or other factors require further investigation.

PARP9, a mono-ADP ribosyl transferase, is not involved in DNA repair [45] but has been linked to the regulation of apoptosis and inflammation in various disease models [21–24]. Our study shows that knockdown of PARP9 alleviated neuroinflammation in the ipsilateral thalamus and hippocampus after focal cerebral infarction, which is consistent with findings in other diseases [18, 24]. Interestingly, while elevated PARP9 levels inhibit apoptosis and promote tumor cell proliferation in cancers [23, 46], the situation appears to differ in the context of stroke. In breast cancer cells, inhibition of PARP9 has been shown to reduce the activity of the PI3K/AKT/PD-L1 axis, promoting apoptosis and thereby ameliorating chemotherapy resistance and immune escape in breast cancer [30]. In contrast, our study found that knockdown of PARP9 activates the PI3K pathway, alleviating neuronal apoptosis in the ipsilateral thalamus and hippocampus after dMCAO, which contrasts with its role in cancer. Current studies indicate that PARP9 acts as an upstream regulator and the PI3K pathway can serve as at least one of the most important downstream targets of PARP9. However, we propose that the ultimate effect of the PARP9-PI3K axis can vary depending on the intermediate signaling molecules involved. In cancer cells, one of such key intermediate molecules is DTX3L, which mediates the regulation of the PI3K pathway by PARP9 [47]. Silencing DTX3L significantly reduces PI3K pathway activity, inhibiting cancer cell proliferation, migration, and invasion [48]. DTX3L complexes play a crucial role in multiple signaling pathways that promote adhesion, proliferation, migration, and chemoresistance in various cancers [49]. These findings suggest that PARP9 exerts its effects in cancer cells through DTX3L-mediated regulation of the PI3K pathway. This discrepancy in the effect of PARP9 on the PI3K pathway between cancer cells and neurons could be due to differences in the intermediate signaling molecules involved. While DTX3L mediates the effects of PARP9 in cancer cells, the specific intermediate molecules involved in PARP9 signaling in stroke remain unclear. These variations in intermediate molecules might help explain the distinct effects of PARP9 on the PI3K pathway in these two contexts. Future studies could identify the specific intermediate molecules involved in PARP9 signaling during stroke to clarify this mechanism. Moreover, while cancer cells evade apoptosis through altered signaling pathways, neurons are more sensitive to stress-induced programmed cell death [50,

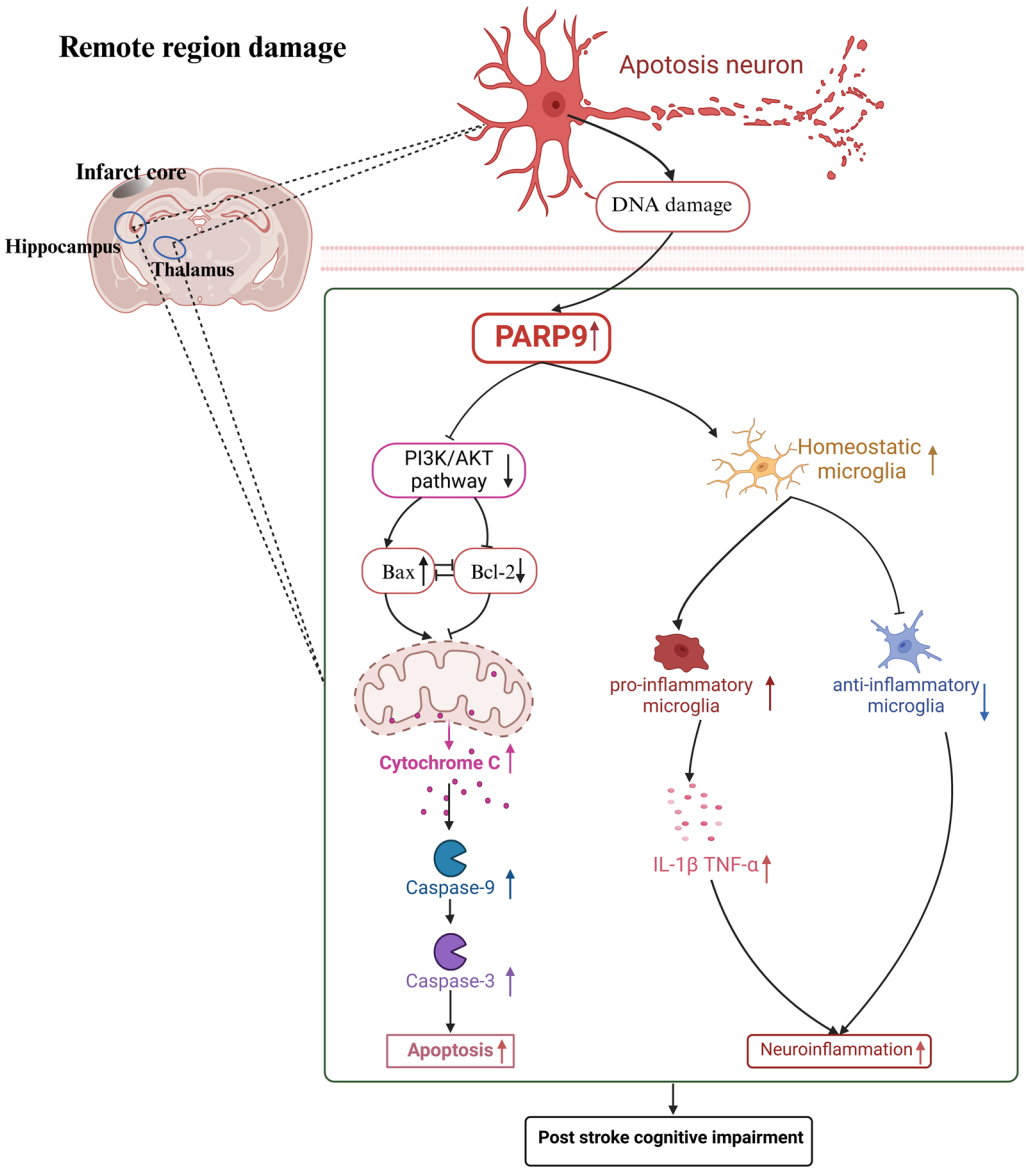

Fig. 8 Schematic summary. After cerebral infarction, elevated PARP9 expression in the ipsilateral thalamus and hippocampus inhibits the PI3K pathway, leading to increased apoptosis and inflammation, which subsequently results in cognitive impairment. Created in BioRender. Liao, M. (2025) https://BioRender.com/p74h554

51]. These molecular response differences between cancer cells and neurons may explain why PARP9 has distinctly different roles in these two contexts. Despite these differences, in both tumor progression and post-stroke conditions, PARP9 acts as a destructive factor. Importantly, our findings suggest that by inhibiting PARP9 overactivation, we can mitigate both apoptosis and neuroinflammation, effectively reducing secondary damage and improving cognitive outcomes in rats after cortical infarction. These results are consistent with prior studies that established the link between alleviating apoptosis or neuroinflammation in remote brain regions and cognitive improvement [52, 53]. Therefore, PARP9 represents a promising therapeutic target for mitigating cognitive impairments associated with cerebral infarction.

Our study found that while overexpression of PARP9 exacerbated neuronal apoptosis and neuroinflammation after cerebral cortical infarction, some effects were statistically significant, whereas others showed a nonsignificant trend. To ensure effective viral transduction, AAV9 encoding PARP9 was stereotactically injected into the right thalamus and hippocampus 8 weeks post-RHRSP

induction, achieving stable expression levels within 4 weeks [54, 55]. As expected, PARP9 expression was further increased in overexpressing rats after dMCAO. However, the abrupt and destructive nature of cerebral infarction leads to significant neuronal loss in remote areas with fiber connections to the primary lesion, resulting in significant secondary damage [1, 56, 57]. While upregulating PARP9 led to increased neuronal apoptosis, neuroinflammation, and secondary damage in these regions, the observed changes were relatively modest compared to the pronounced neuroprotection seen with PARP9 knockdown. This could be due to the fact that the extensive neuronal loss and neuroinflammation induced by the infarction itself had already caused severe damage in the remote regions, leaving limited room for additional effects from PARP9 overexpression to reach statistical significance. Specifically, although AAV-PARP9 intervention led to an increase in the total number of microglia, the pro-inflammatory microglia to anti-inflammatory microglia polarization ratio did not change significantly, suggesting that the proliferating microglia were likely in a quiescent state. This could explain the lack of significant changes in inflammatory cytokines following PARP9 overexpression, as there was no notable increase in the key pro-inflammatory microglial population. Furthermore, overexpression of PARP9 may act as an upstream signaling molecule or gene that, to some extent, regulates downstream pathways and effector molecules through negative feedback mechanisms. This negative feedback could limit the excessive upregulation of inflammatory factors, serving as a protective self-limiting mechanism to prevent excessive neuroinflammation [58, 59].

The PI3K pathway, is well-established for its roles in promoting cell survival [60], regulating apoptosis [61], and modulating inflammation [11], emerging as a critical mechanism through which PARP9 influences neuronal apoptosis and neuroinflammation. In cancer cells, PARP9 overexpression promotes cell proliferation and migration, likely through the activation of the PI3K pathway, which enhances proliferation and metastasis [30]. Similarly, in immune cells, PARP9 overexpression enhances immune responses by activating the PI3K pathway, particularly during viral challenges, thereby promoting immune activation [24, 62]. In contrast, our findings show that PARP9 knockdown significantly increases PI3K, AKT, and mTOR phosphorylation in the ipsilateral thalamus and hippocampus, suggesting a neuroprotective role of this pathway in stroke. This contrasts with the inhibitory role of PARP9 in cancer and immune cells, highlighting the context-dependent nature of its functions. These results suggest that PARP9 regulates the PI3K pathway differently in distinct cell types and contexts, which activates the PI3K pathway in remote brain regions to protect against post-stroke secondary damage while plays inhibitory role in cancer [51] and immune cells [63]. To further confirm this, future studies should explore the use of PI3K inhibitors in cerebral infarction models. Notably, the neuroprotective effects of PARP9 knockdown were partially reversed by the PI3K-specific inhibitor LY294002 [34], which blocked PI3K phosphorylation, reinstated apoptosis, and reactivated inflammation. In conclusion, PARP9 knockdown mediates neuronal apoptosis and neuroinflammation in cerebral infarction, potentially via PI3K pathway activation. While inhibiting PI3K signaling affects apoptosis and inflammation, it does not fully reverse these effects, suggesting the involvement of additional molecular pathways.

Despite the promising findings, this study has several limitations. First, the use of targeted stereotactic injections confined to the ipsilateral thalamus and hippocampus limits our understanding of systemic and regional PARP9 expression dynamics across the CNS and peripheral tissues. Second, while the involvement of the PI3K pathway in PARP9-mediated neuronal apoptosis and inflammation is evident, the specific and direct molecular interactions between PARP9 and this pathway remain unclear. Furthermore, although inhibition of the PI3K pathway significantly impacts neuronal apoptosis and neuroinflammation, it does not fully reverse these effects, suggesting that additional molecular pathways may also contribute. Third, our study did not fully investigate how neuronal PARP9 affects microglial polarization. Given its predominant expression in neurons and low levels in microglia, the effects of PARP9 may be mediated through non-cell-autonomous mechanisms, such as neuron-microglia interactions. Future studies using cell co-culture systems or cell-specific genetic tools (e.g., Cre-loxP) are needed to validate this. Moreover, our research focused on classical pro-inflammatory and anti-inflammatory microglia markers, which may not fully capture the complexity of microglial polarization. The role of neuronal PARP9 in microglial polarization is still in its early stages, and future studies should explore a broader range of microglial phenotypes, including non-canonical states by means of single-cell RNA sequencing and spatial transcriptomics. Additionally, the relatively small sample size may limit the statistical power and generalizability of our results, highlighting the need for larger-scale studies to confirm these findings. Finally, our study did not assess long-term cognitive function, which remains an important area for future research.

Conclusions

This study demonstrates that PARP9 expression is significantly upregulated in the ipsilateral nonischemic thalamus and hippocampus in hypertensive rats after

cerebral cortical infarction. PARP9 knockdown alleviates neuronal apoptosis and neuroinflammation by activating the PI3K pathway, contributing to recovery from secondary brain damage and improving cognitive impairment in remote regions after dMCAO. These findings position PARP9 as a key mediator in post-stroke pathology and may shed light on the therapeutic implications of PARP9 in mitigating secondary brain damage and cognitive decline after cerebral infarction.

Abbreviations

RHRSP	Renovascular hypertensive rat stroke-prone
dMCAO	Distal middle cerebral artery occlusion
PARP9	Poly (ADP-ribose) polymerase 9
AAV	Adeno-associated virus
NeuN	Neuronal nuclear protein
Iba-1	Ionized calcium-binding adapter molecule 1
GFAP	Glial fibrillary acidic protein
GFP	Green fluorescent protein; TNF-α
TNF-α	Tumor necrosis factor α
IL-1β	Interleukin-1β
CC3	Cleaved caspase-3
CC9	Cleaved caspase-9
p-PI3K	Phosphorylated phosphoinositide 3-kinase
p-AKT	Phosphorylated protein kinase B
p-mTOR	Phosphorylated mammalian target of rapamycin
TUNEL	Terminal deoxynucleotidyl transferase dUTP nick end labeling
mRNA-seq	Messenger RNA Sequencing
LY294002	2-(4-morpholinyl)-8-phenyl-chromone

Supplementary Information

The online version contains supplementary material available at https://doi.org/10.1186/s12974-025-03374-x.

Supplementary material 1: Figure S1. Experimental Timeline. Part 1: dMCAO or Sham-operated group. Part 2: PARP9 modulation or respective negative control group. Part 3: PARP9 inhibition combined with PI3K inhibition or vehicle group. Figure S2. Animal Experimental Design Flowchart. The renovascular hypertensive rat stroke-pronemodel was established, after which rats were divided into groups. At 8 weeks, adeno-associated viruswas injected into the right thalamus and hippocampus, followed by distal middle cerebral artery occlusionat 12 weeks. Behavioral assessments, including the Bederson and Garcia scores, along with the Morris water maze test, were conducted between weeks 12 and 13. Following the behavioral tests, brain tissue was collected for molecular and histological analyses, including Western blot, Nissl staining, immunofluorescence, and TUNEL staining. Figure S3. Secondary brain damage and cognitive impairment after dMCAO.Representative macroscopic anatomical images and Nissl staining of rat brains after dMCAO. Infarct areas are indicated by stars and triangles.Trajectories in the Morris water maze for Sham and dMCAO groups, illustrating spatial learning deficits after dMCAO.Quantitative analysis of escape latency from days 3 to 6 in the Morris water maze, reflecting cognitive function.Time spent in the target quadrant during the day 7 probe trial, assessing spatial memory performance.Representative Nissl-stained images of the thalamus and hippocampal CA3 region on the lesioned side in Sham and dMCAO groups. Scale bar=50 μm.Semi-quantitative analysis of Nissl-positive neurons in the thalamus and hippocampal CA3 region on the lesioned side for both groups.Modified Bederson and Garcia scores for Sham and dMCAO groups, reflecting neurological deficits. Data are presented as mean ± SEM. *p < 0.05 compared to the Sham group. Figure S4. Neuronal apoptosis and neuroinflammation in the ipsilateral hippocampal CA3 region after dMCAO.Representative immunofluorescence images showing co-localization of cleaved caspase-3, NeuN, and DAPI, and separate co-localization of CD86with Iba-1in the ipsilateral hippocampal CA3 region of sham-operated and dMCAO rats. Scale bar = 50 μm, n=4 per group.Quantitative analysis of NeuN-positive neurons, CC3-positive neurons, Iba-1-positive microglia, and CD86-positive microgliain the ipsilateral hippocampal CA3 region, with comparisons to sham-operated groups.Western blot analysis of cleaved caspase-9, caspase-9, Bax, Bcl-2, TNF-α, and IL-1β protein levels in the ipsilateral hippocampal CA3 region of sham-operated and dMCAO rats. Semi-quantitative analysis of protein expression, with CC9 normalized to caspase-9, and Bax, Bcl-2, TNF-α, and IL-1β normalized to α-tubulin. Data are presented as mean ± SEM. *p < 0.05, compared to the sham-operated group.Representative immunofluorescence images showing co-localization of CD163with Iba-1in the ipsilateral thalamus and hippocampal CA3 region of sham-operated and dMCAO rats. Scale bar = 50 μm, n = 4 per group.Quantitative analysis of CD163-positive microgliain the ipsilateral thalamus and hippocampal CA3 region, compared to the sham-operated groups. Figure S5. Spatial expression patterns of PARP9 in the ipsilateral thalamus and hippocampus after dMCAO.Western blot analysis of PARP9 expression in the ipsilateral hippocampus of sham-operated and dMCAO groups.Quantitative analysis of PARP9 expression normalized to α-tubulin, comparing sham-operated and dMCAO groups. Data are presented as mean ± SEM, n = 3 per group.Western blot analysis of PARP9 expression in the ipsilateral thalamus and hippocampus at 3, 7, and 14 days post-dMCAO, compared to sham-operated rats.Quantitative analysis of PARP9 expression normalized to α-tubulin, comparing sham-operated and 3, 7, and 14 days post-dMCAO. Data are presented as mean ± SEM, n = 3 per group.Representative immunohistochemical images showing PARP9 expression in the ipsilateral and contralateral thalamus, as well as the hippocampal CA3 region of sham-operated and dMCAO rats. Scale bar = 50 μm.Quantitative analysis of mean optical density values for PARP9 in both groups. n = 4 per group. Data are presented as mean ±SEM. *p < 0.05, versus the sham-operated group. Figure S6. AAV-mediated knockdown and overexpression of PARP9 in the ipsilateral hippocampus after dMCAO.Schematic of brain sectionshowing cortical infarction areaand ipsilateral thalamus.Whole-brain immunofluorescence images displaying GFP-tagged AAV distribution in brain slices 7 days after dMCAO, with 4x magnified views of the ipsilateral thalamus and hippocampus. Scale bar=400 μm.Immunofluorescence images showing co-localization of GFPwith NeuN, Iba-1, GFAP, and DAPIin the ipsilateral hippocampus. Scale bar: 50 μm.Western blot images showing PARP9 and α-tubulin expression in the ipsilateral hippocampus from AAV-siScramble, AAV-siPARP9, AAV-Scramble, and AAV-PARP9 groups, with semi-quantitative analysis of PARP9 expression relative to α-tubulin. Data are presented as mean ± SEM. *p < 0.05, compared with respective control groups. Figure S7. Effects of PARP9 expression on motor and sensory functions after dMCAO.Number of platform crossings on day 7 post-dMCAO for the AAV-siScramble, AAV-siPARP9, AAV-Scramble, and AAV-PARP9 groups.Statistical analysis of average swimming speed from days 3 to 6 post-dMCAO across the four groups.Modified Bederson score and Garcia score results for the four groups. Data are presented as mean ± SEM. *p < 0.05 compared to the respective negative control group. Figure S8. Effects of PARP9 knockdown or overexpression on neuronal apoptosis in the ipsilateral hippocampus after dMCAO.Representative images of TUNEL staining and co-immunofluorescence staining for cleaved caspase-3, NeuN, and DAPIin the ipsilateral hippocampal CA3 region across AAV-siScramble, AAV-siPARP9, AAV-Scramble, and AAV-PARP9 groups. Scale bar = 50 μm.Quantitative analysis of TUNEL-positive cells and CC3-positive neurons in the ipsilateral hippocampal CA3 region.Representative Western blot images showing expression levels of cleaved caspase-9, total caspase-9, Bax, Bcl-2, and α-tubulin in the ipsilateral hippocampus at 7 days after dMCAO across groups.Semi-quantitative analysis of CC9 normalized to total caspase-9, and Bax and Bcl-2 normalized to α-tubulin. n = 3 per group. Data are presented as mean ± SEM. *p < 0.05 compared with the respective scramble control group. Figure S9. Effects of PARP9 knockdown or overexpression on neuroinflammation in the ipsilateral hippocampus after dMCAO.Representative immunofluorescence images showing co-staining of Iba-1with CD86and CD163in the ipsilateral hippocampal CA3 region across AAV-siScramble, AAV-siPARP9, AAV-Scramble, and AAV-PARP9 groups. Scale bar = 50 μm. Quantitative analysis of total microglial countsand CD86-positive

microglia, and CD163-positive microgliain the ipsilateral hippocampal CA3 region across the four groups.Representative Western blot images showing IL-1β, TNF-α, and α-tubulin expression in the ipsilateral hippocampus 7 days after dMCAO across the four groups.Semi-quantitative analysis of IL-1β and TNF-α protein levels, normalized to α-tubulin. n = 3 per group. Data are presented as mean ± SEM. *p < 0.05, compared to the respective scramble control group. Figure S10. Effects of LY294002 on motor and sensory functions in PARP9 knockdown rats.Number of platform crossings on day 7 post-dMCAO for the siPARP9-vehicle and siPARP9-LY294002 groups.Statistical analysis of average swimming speed from days 3 to 6 post-dMCAO in both groups.Modified Bederson and Garcia scores for the two groups. Data are presented as mean ± SEM. *p < 0.05 compared to the vehicle control group. Figure S11. Inhibition of the PI3K pathway in the hippocampus following PARP9 knockdown after dMCAO.Western blot images showing p-PI3K, PI3K, p-AKT, AKT, p-mTOR, mTOR, and GAPDH in the ipsilateral hippocampus of siPARP9-vehicle and siPARP9-LY294002 groups.Quantitative analysis of p-PI3K, p-AKT, and p-mTOR normalized to total protein.Western blot images of p-AKT, AKT, p-mTOR, mTOR, Bax, Bcl-2, CC9, caspase-9, TNF-α, IL-1β, and α-tubulin. Semi-quantitative analysis of P-AKT, P-mTOR, and CC9 normalized to total protein, with Bax, Bcl-2, TNF-α, and IL-1β normalized to α-tubulin. Data are presented as mean ± SEM. *p < 0.05 compared to vehicle group.

Supplementary material 2

Acknowledgements
Not applicable.

Author contributions
Mengshi Liao contributed to the study's conception and design, performed the experiments, conducted statistical analyses, and drafted and revised the manuscript. Xiya Long, Yicong Chen, and Jiaqi An contributed to the experimental design and conducted the experiments. Weixian Huang and Xiangming Xu assisted with the experiments. Yuhua Fan oversaw the study's conception and design and provided significant revisions to the manuscript.

Funding
This work was supported by grants from the National Natural Science Foundation of China (82071294) and the Guangzhou Science and Technology Program Key Project (202007030010).

Availability of data and materials
No datasets were generated or analysed during the current study.

Declarations

Ethics approval and consent to participate
All animal experiments in the study were approved by the Institutional Animal Care and Use Committee, Sun Yat-Sen university.

Consent for publication
Not applicable.

Competing interests
The authors declare no competing interests.

Author details
[1]Department of Neurology, Guangdong Provincial Key Laboratory for Diagnosis and Treatment of Major Neurological Diseases, National Key Clinical Department and Key Discipline of Neurology, The First Affiliated Hospital, Sun Yat-Sen University, Guangzhou, China. [2]Department of Neurology, Guangdong Provincial People's Hospital, Southern Medical University, Guangzhou, China.

Received: 14 December 2024 Accepted: 10 February 2025
Published online: 20 February 2025

References

1. Zhang J, Zhang Y, Xing S, Liang Z, Zeng J. Secondary neurodegeneration in remote regions after focal cerebral infarction: a new target for stroke management? Stroke. 2012;43:1700–5.
2. Weaver NA, Kuijf HJ, Aben HP, Abrigo J, Bae H-J, Barbay M, Best JG, Bordet R, Chappell FM, Chen CPLH, et al. Strategic infarct locations for post-stroke cognitive impairment: a pooled analysis of individual patient data from 12 acute ischaemic stroke cohorts. Lancet Neurol. 2021;20:448–59.
3. Freret T, Chazalviel L, Roussel S, Bernaudin M, Schumann-Bard P, Boulouard M. Long-term functional outcome following transient middle cerebral artery occlusion in the rat: correlation between brain damage and behavioral impairment. Behav Neurosci. 2006;120:1285–98.
4. Stuckey SM, Ong LK, Collins-Praino LE, Turner RJ. Neuroinflammation as a key driver of secondary neurodegeneration following stroke? Int J Mol Sci. 2021;22:13101.
5. Chen Y, Veenman L, Singh S, Ouyang F, Liang J, Huang W, Marek I, Zeng J, Gavish M. 2-Cl-MGV-1 ameliorates apoptosis in the thalamus and hippocampus and cognitive deficits after cortical infarct in rats. Stroke. 2017;48:3366–74.
6. Xing S, Zhang J, Dang C, Liu G, Zhang Y, Li J, Fan Y, Pei Z, Zeng J. Cerebrolysin reduces amyloid-β deposits, apoptosis and autophagy in the thalamus and improves functional recovery after cortical infarction. J Neurol Sci. 2014;337:104–11.
7. Li W-H, Yang Y-L, Cheng X, Liu M, Zhang S-S, Wang Y-H, Du G-H. Baicalein attenuates caspase-independent cells death via inhibiting PARP-1 activation and AIF nuclear translocation in cerebral ischemia/reperfusion rats. Apoptosis. 2020;25:354–69.
8. Block F, Dihné M, Loos M. Inflammation in areas of remote changes following focal brain lesion. Prog Neurobiol. 2005;75:342–65.
9. Wang M, Pan W, Xu Y, Zhang J, Wan J, Jiang H. Microglia-mediated neuroinflammation: a potential target for the treatment of cardiovascular diseases. J Inflamm Res. 2022;15:3083–94.
10. Wang Y, Tian M, Tan J, Pei X, Lu C, Xin Y, Deng S, Zhao F, Gao Y, Gong Y. Irisin ameliorates neuroinflammation and neuronal apoptosis through integrin αVβ5/AMPK signaling pathway after intracerebral hemorrhage in mice. J Neuroinflamm. 2022;19:82.
11. Tian Q, Guo Y, Feng S, Liu C, He P, Wang J, Han W, Yang C, Zhang Z, Li M. Inhibition of CCR2 attenuates neuroinflammation and neuronal apoptosis after subarachnoid hemorrhage through the PI3K/Akt pathway. J Neuroinflamm. 2022;19:312.
12. Vyas S, Chesarone-Cataldo M, Todorova T, Huang Y-H, Chang P. A systematic analysis of the PARP protein family identifies new functions critical for cell physiology. Nat Commun. 2013;4:2240.
13. Koehler RC, Dawson VL, Dawson TM. Targeting parthanatos in ischemic stroke. Front Neurol. 2021;12:662034.
14. Liu S, Luo W, Wang Y. Emerging role of PARP-1 and PARthanatos in ischemic stroke. J Neurochem. 2022;160:74–87.
15. Stoica BA, Loane DJ, Zhao Z, Kabadi SV, Hanscom M, Byrnes KR, Faden AI. PARP-1inhibition attenuates neuronal loss, microglia activation and neurological deficits after traumatic brain injury. J Neurotrauma. 2014;31:758–72.
16. Wang Y, An R, Umanah GK, Park H, Nambiar K, Eacker SM, Kim B, Bao L, Harraz MM, Chang C, et al. A nuclease that mediates cell death induced by DNA damage and poly(ADP-ribose) polymerase-1. Science. 2016;354:6308.
17. Riffell JL, Lord CJ, Ashworth A. Tankyrase-targeted therapeutics: expanding opportunities in the PARP family. Nat Rev Drug Discov. 2012;11:923–36.
18. Iwata H, Goettsch C, Sharma A, Ricchiuto P, Goh WWB, Halu A, Yamada I, Yoshida H, Hara T, Wei M, et al. PARP9 and PARP14 cross-regulate macrophage activation via STAT1 ADP-ribosylation. Nat Commun. 2016;7:12849.
19. Tang Y, Liu J, Wang Y, Yang L, Han B, Zhang Y, Bai Y, Shen L, Li M, Jiang T, et al. PARP14 inhibits microglial activation via LPAR5 to promote post-stroke functional recovery. Autophagy. 2021;17:2905–22.
20. Hakmé A, Huber A, Dollé P, Schreiber V. The macroPARP genes Parp-9 and Parp-14 are developmentally and differentially regulated in mouse tissues. Dev Dyn. 2008;237:209–15.
21. Xu H, Chai S, Wang Y, Wang J, Xiao D, Li J, Xiong N. Molecular and clinical characterization of PARP9 in gliomas: a potential immunotherapeutic target. CNS Neurosci Ther. 2020;26:804–14.

22. Zhu H, Wu L-F, Mo X-B, Lu X, Tang H, Zhu X-W, Xia W, Guo Y-F, Wang M-J, Zeng K-Q, et al. Rheumatoid arthritis-associated DNA methylation sites in peripheral blood mononuclear cells. Ann Rheum Dis. 2019;78:36–42.
23. Camicia R, Bachmann SB, Winkler HC, Beer M, Tinguely M, Haralambieva E, Hassa PO. BAL1/ARTD9 represses the anti-proliferative and pro-apoptotic IFNγ-STAT1-IRF1-p53 axis in diffuse large B-cell lymphoma. J Cell Sci. 2013;126:1969–80.
24. Xing J, Zhang A, Du Y, Fang M, Minze LJ, Liu Y-J, Li XC, Zhang Z. Identification of poly(ADP-ribose) polymerase 9 (PARP9) as a noncanonical sensor for RNA virus in dendritic cells. Nat Commun. 2021;12:2681.
25. Fruman DA, Chiu H, Hopkins BD, Bagrodia S, Cantley LC, Abraham RT. The PI3K pathway in human disease. Cell. 2017;170:605–35.
26. Lin J-Y, Kuo W-W, Baskaran R, Kuo C-H, Chen Y-A, Chen WS-T, Ho T-J, Day CH, Mahalakshmi B, Huang C-Y. Swimming exercise stimulates IGF1/ PI3K/Akt and AMPK/SIRT1/PGC1α survival signaling to suppress apoptosis and inflammation in aging hippocampus. Aging. 2020;12:6852–64.
27. Liu Y, Gong S, Li K, Wu G, Zheng X, Zheng J, Lu X, Zhang L, Li J, Su Z, et al. Coptisine protects against hyperuricemic nephropathy through alleviating inflammation, oxidative stress and mitochondrial apoptosis via PI3K/Akt signaling pathway. Biomed Pharmacother = Biomed Pharmacother. 2022;156:113941.
28. Ates N, Caglayan A, Balcikanli Z, Sertel E, Beker MC, Dilsiz P, Caglayan AB, Celik S, Dasdelen MF, Caglayan B, et al. Phosphorylation of PI3K/Akt at Thr308, but not phosphorylation of MAPK kinase, mediates lithium-induced neuroprotection against cerebral ischemia in mice. Exp Neurol. 2022;351:113996.
29. Feng C, Wan H, Zhang Y, Yu L, Shao C, He Y, Wan H, Jin W. Neuroprotective effect of danhong injection on cerebral ischemia-reperfusion injury in rats by activation of the PI3K-Akt pathway. Front Pharmacol. 2020;11:298.
30. Hong T, Dong D, Li J, Wang L. PARP9 knockdown confers protection against chemoresistance and immune escape of breast cancer cells by blocking the PI3K/AKT pathway. Arch Med Sci AMS. 2024;20:1228–48.
31. Zeng J, Zhang Y, Mo J, Su Z, Huang R. Two-kidney, two clip renovascular hypertensive rats can be used as stroke-prone rats. Stroke. 1998;29:1708.
32. Brint S, Jacewicz M, Kiessling M, Tanabe J, Pulsinelli W. Focal brain ischemia in the rat: methods for reproducible neocortical infarction using tandem occlusion of the distal middle cerebral and ipsilateral common carotid arteries. J Cereb Blood Flow Metab. 1988;8:474–85.
33. Xing S, Zhang Y, Li J, Zhang J, Li Y, Dang C, Li C, Fan Y, Yu J, Pei Z, Zeng J. Beclin 1 knockdown inhibits autophagic activation and prevents the secondary neurodegenerative damage in the ipsilateral thalamus following focal cerebral infarction. Autophagy. 2012;8:63–76.
34. Md Mokhtar AH, Malik IA, Abd Aziz NAA, Almabhouh FA, Durairajanayagam D, Singh HJ. LY294002, a PI3K pathway inhibitor, prevents leptin-induced adverse effects on spermatozoa in Sprague-Dawley rats. Andrologia. 2019;51: e13196.
35. Kerenyi SZ, Hartgraves SL. Premature excess release from the Alzet osmotic pump. Pharmacol Biochem Behav. 1987;27:199–201.
36. Xiao P, Gu J, Xu W, Niu X, Zhang J, Li J, Chen Y, Pei Z, Zeng J, Xing S. RTN4/Nogo-A-S1PR2 negatively regulates angiogenesis and secondary neural repair through enhancing vascular autophagy in the thalamus after cerebral cortical infarction. Autophagy. 2022;18:2711–30.
37. Vorhees CV, Williams MT. Morris water maze: procedures for assessing spatial and related forms of learning and memory. Nat Protoc. 2006;1:848–58.
38. Bederson JB, Pitts LH, Tsuji M, Nishimura MC, Davis RL, Bartkowski H. Rat middle cerebral artery occlusion: evaluation of the model and development of a neurologic examination. Stroke. 1986;17:472–6.
39. Garcia JH, Wagner S, Liu KF, Hu XJ. Neurological deficit and extent of neuronal necrosis attributable to middle cerebral artery occlusion in rats Statistical validation. Stroke. 1995;26:627.
40. Zhang B, Gu J, Wang Y, Guo L, Xie J, Yang M. TNF-α stimulated exosome derived from fibroblast-like synoviocytes isolated from rheumatoid arthritis patients promotes HUVEC migration, invasion and angiogenesis by targeting the miR-200a-3p/KLF6/VEGFA axis. Autoimmunity. 2023;56:2282939.
41. Dihné M, Grommes C, Lutzenburg M, Witte OW, Block F. Different mechanisms of secondary neuronal damage in thalamic nuclei after focal cerebral ischemia in rats. Stroke. 2002;33:3006–11.
42. Jayaraj RL, Azimullah S, Beiram R, Jalal FY, Rosenberg GA. Neuroinflammation: friend and foe for ischemic stroke. J Neuroinflamm. 2019;16:142.
43. Liu C, Shen Y, Tang Y, Gu Y. The role of N-glycosylation of CD200-CD200R1 interaction in classical microglial activation. J Inflamm. 2018;15:28.
44. Mao M, Xu Y, Zhang X-Y, Yang L, An X-B, Qu Y, Chai Y-N, Wang Y-R, Li T-T, Ai J. MicroRNA-195 prevents hippocampal microglial/macrophage polarization towards the M1 phenotype induced by chronic brain hypoperfusion through regulating CX3CL1/CX3CR1 signaling. J Neuroinflammation. 2020;17:244.
45. Gibson BA, Kraus WL. New insights into the molecular and cellular functions of poly(ADP-ribose) and PARPs. Nat Rev Mol Cell Biol. 2012;13:411–24.
46. Tang X, Zhang H, Long Y, Hua H, Jiang Y, Jing J. PARP9 is overexpressed in human breast cancer and promotes cancer cell migration. Oncol Lett. 2018;16:4073–7.
47. Saleh H, Liloglou T, Rigden DJ, Parsons JL, Grundy GJ. KH-like domains in PARP9/DTX3L and PARP14 coordinate protein-protein interactions to promote cancer cell survival. J Mol Biol. 2024;436:168434.
48. Hu W, Hu Y, Pei Y, Li R, Xu F, Chi X, Mi J, Bergquist J, Lu L, Zhang L, Yang C. Silencing DTX3L inhibits the progression of cervical carcinoma by regulating PI3K/AKT/mTOR signaling pathway. Int J Mol Sci. 2023;24:861.
49. Vela-Rodríguez C, Lehtiö L. Activities and binding partners of E3 ubiquitin ligase DTX3L and its roles in cancer. Biochem Soc Trans. 2022;50:1683–92.
50. Wang F, Wu P, Qin S, Deng Y, Han P, Li X, Fan C, Xu Y. Curcin C inhibit osteosarcoma cell line U2OS proliferation by ROS induced apoptosis, autophagy and cell cycle arrest through activating JNK signal pathway. Int J Biol Macromol. 2022;195:433–9.
51. Yuan J, Ofengeim D. A guide to cell death pathways. Nat Rev Mol Cell Biol. 2024;25:379–95.
52. Brainin M, Tuomilehto J, Heiss WD, Bornstein NM, Bath PMW, Teuschl Y, Richard E, Guekht A, Quinn T. Post-stroke cognitive decline: an update and perspectives for clinical research. Eur J Neurol. 2015;22:229.
53. Fernández-Andújar M, Doornink F, Dacosta-Aguayo R, Soriano-Raya JJ, Miralbell J, Bargalló N, López-Cancio E, Pérez de la Ossa N, Gomis M, Millán M, et al. Remote thalamic microstructural abnormalities related to cognitive function in ischemic stroke patients. Neuropsychology. 2014;28:984–96.
54. Chai Z, Zhang X, Dobbins AL, Samulski RJ, Merricks EP, Nichols TC, Li C. Dexamethasone transiently enhances transgene expression in the liver when administered at late-phase post long-term adeno-associated virus transduction. Hum Gene Ther. 2022;33:119–30.
55. Mitroshina EV, Mishchenko TA, Usenko AV, Epifanova EA, Yarkov RS, Gavrish MS, Babaev AA, Vedunova MV. AAV-Syn-BDNF-EGFP virus construct exerts neuroprotective action on the hippocampal neural network during hypoxia in vitro. Int J Mol Sci. 2018;19:2295.
56. Karan AA, Spivak YS, Suleymanova EM, Gerasimov KA, Bolshakov AP, Vinogradova LV. Distant neuroinflammation acutely induced by focal brain injury and its control by endocannabinoid system. Exp Neurol. 2024;373:114679.
57. Liang Z, Zeng J, Liu S, Ling X, Xu A, Yu J, Ling L. A prospective study of secondary degeneration following subcortical infarction using diffusion tensor imaging. J Neurol Neurosurg Psychiatry. 2007;78:581–6.
58. Jiang K, Zhang Y, He F, Zhang M, Li T, Tu Z, Xu D, Zhang M, Han L, Guo L, et al. A negative feedback loop involving NF-κB/TIR8 regulates IL-1β-induced epithelial- myofibroblast transdifferentiation in human tubular cells. J Cell Commun Signal. 2021;15:393–403.
59. Li Z, Zhang K, Li X, Pan H, Li S, Chen F, Zhang J, Zheng Z, Wang J, Liu H. Wnt5a suppresses inflammation-driven intervertebral disc degeneration via a TNF-α/NF-κB-Wnt5a negative-feedback loop. Osteoarthr Cartil. 2018;26:966–77.
60. Zhang J-J, Li Y, Chen S, Yang X-F, Min J-W. Biphalin, a dimeric opioid peptide, reduces neonatal hypoxia-ischemia brain injury in mice by the activation of PI3K/Akt signaling pathway. J Chem Neuroanat. 2021;115:101967.
61. Yang J, Pi C, Wang G. Inhibition of PI3K/Akt/mTOR pathway by apigenin induces apoptosis and autophagy in hepatocellular carcinoma cells. Biomed Pharmacother = Biomed Pharmacother. 2018;103:699–707.
62. Pandi K, Angabo S, Makkawi H, Benyamini H, Elgavish S, Nussbaum G. P. gingivalis-induced TLR2 interactome analysis reveals association with PARP9. J Dent Res. 2024;103:329–38.
63. Okkenhaug K. Signaling by the phosphoinositide 3-kinase family in immune cells. Annu Rev Immunol. 2013;31:675–704.